Article

Tribocorrosion behaviour of γ′-Fe_4N nitride layer formed on mild steel by plasma nitriding in chloride containing solution

Yong Sun* and Richard Bailey

School of Engineering and Sustainable Development, Faculty of Computing, Engineering and Media, De Montfort University, Leicester LE1 9BH, UK

* Correspondence: Corresponding author: email: ysun01@dmu.ac.uk

Abstract: Nitriding has long been used to engineer the surfaces of engineering steels to improve their surface and subsurface properties. The role of the surface compound layer (γ′-Fe_4N and/or ε-$Fe_{2-3}N$) in improving the tribological and corrosion resistant properties of nitrided steels has been established. However, there have been very few studies on the response of the compound layer to tribocorrosion in corrosive environments. In this work, the tribocorrosion behaviour of a 5 μm thick γ′-Fe_4N nitride layer produced on mild steel (MS) by plasma nitriding has been studied in a NaCl containing solution under various electrochemical conditions. The results show that at a cathodic potential, where mechanical wear is predominant, the total material removal (TMR) from the γ′-Fe_4N layer is 37% smaller than that from the untreated MS, and at open circuit potential, TMR from the layer is 35% smaller than that from the untreated MS, while at an anodic potential, the γ′-Fe_4N layer can reduce TMR from mild steel by 87%. The beneficial effect of the γ′-Fe_4N nitride layer in improving the tribocorrosion behaviour of mild steel is derived from its high hardness and good corrosion resistance in the test solution and its ability to resist both mechanical wear and chemical wear.

Keywords: Nitriding; iron nitride; wear; corrosion; tribocorrosion; mild steel

1. Introduction

Nitriding is a common thermochemical treatment technique used to engineer the surfaces of engineering steels [1-5] and many other metallic materials like titanium alloys [6,7], aluminium alloys [8,9], nickel-based alloys [10,11] and Co-Cr biomedical alloys [12,13]. In particular, nitriding has long been used in industry to case-harden many steel components such as gears and drive-shafts to improve their performance and durability in real applications [1,2]. This is due to the formation of an iron nitride compound layer on the surface and a nitrogen diffusion zone at the subsurface, which can enhance the wear resistance, fatigue resistance and in many cases corrosion resistance of steel components [1,14].

During nitriding iron and steels, depending on the nitrogen potential or activity in the treatment media and the steel composition, a compound layer of a few microns thick composed of a single γ′-Fe_4N phase, or a mixed γ′-Fe_4N and ε-$Fe_{2-3}N$ phases is formed at the surface [2,3,4]. This is followed by a relatively thick nitrogen diffusion zone at the subsurface. If the steel contains nitriding forming elements such as Cr and V, fine precipitates of nitrides of the alloying elements, such as CrN and VN, will form in the diffusion zone to induce precipitation hardening which contributes to the hardening effect of the diffusion zone [3,15]. In pure iron and plain carbon steels like mild steels, γ′-Fe_4N needles or thin plates form in the diffusion zone, which provide marginal hardening effect [15,16]. In such steels, the surface hardening effect is mainly imparted by the iron nitride compound layer at the surface.

The role of the surface compound layer (γ′-Fe_4N and/or ε-$Fe_{2-3}N$) and the nitrogen diffusion zone in improving the tribological, fatigue and load bearing capacity properties

 doi:10.20944/preprints202305.2018.v1

of nitrided steels has been established [17-20]. The iron nitride compound layer at the surface provides anti-galling properties and good wear resistance, while the nitrogen diffusion zone provides load bearing capacity and enhances the fatigue strength of steel components, due to the hardening effect and compressive residual stresses [17,19]. In general, a single γ′-Fe_4N phase compound layer of a few microns thick is preferred, because a thick compound layer or a mixed phase compound layer can increase the embrittlement of the surface layer which tends to spall off during service [1,2,3]. There have also been reports that the iron nitride compound layer can improve the corrosion resistance of steels, such that nitrided steels can be used in more harsh environmental conditions [14,21,22]. Indeed, in many engineering applications, such as in marine and off-shore applications, nitrided components are used in corrosive environments under mechanical contact sliding conditions. Under such conditions, the components are subjected to combined corrosion and mechanical wear actions, i.e. tribocorrosion [23,24,25]. So far, the studies on the tribocorrosion behaviour of nitrided steels have been focused on stainless steels [26,27]. Although there have been a few studies on the tribocorrosion behaviour of nitrided low alloy steels [28,29], the response of the γ′-Fe_4N compound layer to tribocorrosion has not been fully understood. Due to the importance of such a compound layer in determining the performance of nitrided steels, it is necessary to investigate the tribocorrosion behaviour of the γ′-Fe_4N layer under various electrochemical conditions.

In the present work, a 5 μm thick γ′-Fe_4N iron nitride layer was produced on mild steel (MS) by plasma nitriding. The tribocorrosion behaviour of this γ′-Fe_4N layer was investigated in 1.0% NaCl solution under combined reciprocating sliding wear and electrochemical corrosion conditions. The obtained results are presented and discussed in this paper.

2. Materials and Methods

2.1. Substrate material and plasma nitriding

The substrate material was AISI 1020 mild steel with a carbon content of 0.2 wt%. Low carbon steel was used to ensure the formation of a pure γ′-Fe_4N layer on the surface by controlled plasma nitriding. The steel was in a normalised state with a ferrite + pearlite structure (Figure 1a). Specimens of 25 x 15 x 4 mm dimensions were machined from a steel plate. The surface to be nitrided (25 x 15 mm) was manually ground using SiC grinding papers down to the P1200 grade to achieve a surface finish of 0.2 μm (R_a).

Plasma nitriding was carried out at 550 ℃ in a plasma atmosphere containing 10% N_2 and 90% H_2, at a treatment pressure of 3 mbar for 5 hours. Before nitriding, the surface was cleaned in running water and then in ethanol ultrasonically for 10 min. After plasma nitriding, the specimens were cooled inside the furnace under vacuum (0.1 mbar) down to room temperature.

Figure 1 shows the cross-sectional morphology of the nitrided specimen. Table 1 summarizes the structural features of the nitrided (PN) and un-nitrided (raw) specimens. It can be seen that plasma nitriding produced a thin "white layer" about 5 μm thick at the surface (Figure 1b) and a relatively thick diffusion zone about 300 μm thick beneath (Figure 1a). X-ray diffraction analysis confirmed that the "white layer" at the surface was composed of γ′-Fe_4N phase. In the nitrogen diffusion zone, γ′-Fe_4N needles were formed, which is typical of nitriding pure iron and low carbon steels [15,16]. The surface hardness of the PN and raw specimens were also measured under various indentation loads, and the results are listed in Table 1. Clearly, the nitrided surface exhibited a higher hardness than the un-nitrided surface. At the small indentation load of 25 g, the surface hardness of the PN specimen was 760 HV, which agrees with the reported hardness value of γ′-Fe_4N [30]. With increasing indentation load, the surface hardness of the PN specimen declined quickly, due to increasing substrate effect. This also suggests that the precipitation of γ′-Fe_4N needles in the diffusion zone had limited hardening effect. Thus, the surface hardening effect was mainly derived from the formation of the γ′-Fe_4N layer.

Preprints (www.preprints.org) | NOT PEER-REVIEWED | Posted: 29 May 2023 doi:10.20944/preprints202305.2018.v1

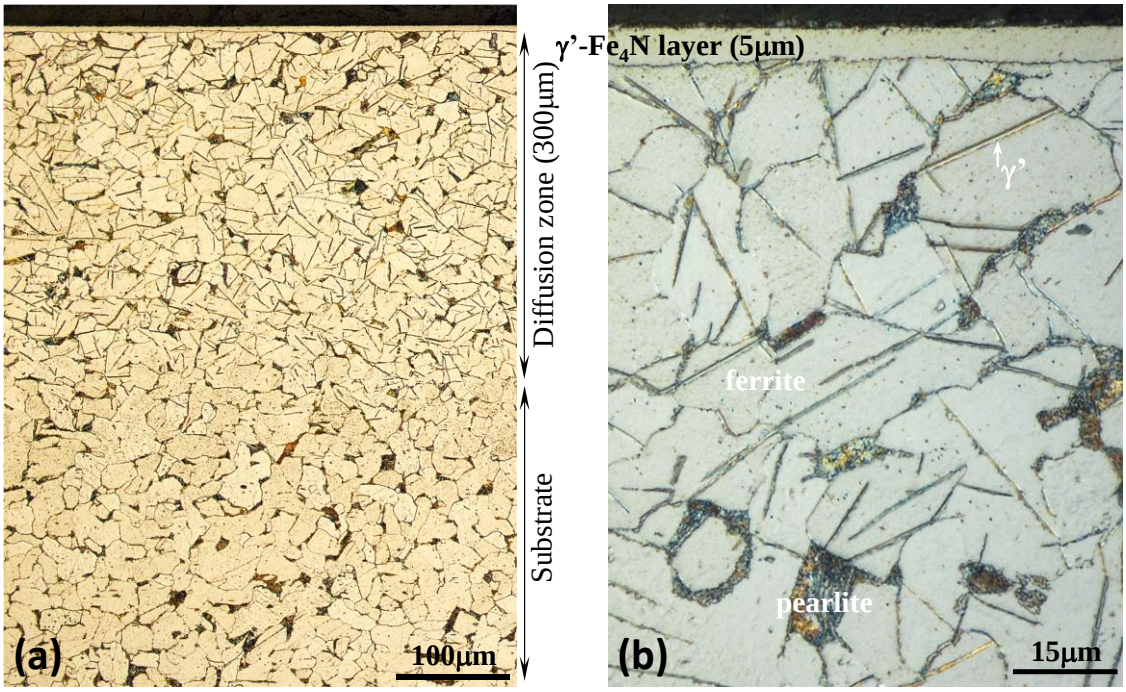

Figure 1. Microscopic images of the nitrided mild steel specimen showing (a) the overall view of the cross section from the surface to the substrate and (b) details of the 5 µm thick Fe_4N compound layer at the surface and the underneath diffusion zone with needle-like precipitates.

Table 1. Summary of structure and surface hardness of the test specimens.

	Structure		Surface Hardness			
Specimen	Surface layer	Diffusion zone	$HV_{0.025}$	$HV_{0.05}$	$HV_{0.1}$	$HV_{0.2}$
PN MS	γ'-Fe_4N 5 µm thick	γ'-Fe_4N needles in α+P matrix	760	540	370	292
Raw MS	α+P	α+P	266	258	248	245

Note: a – Ferrite; P – Pearlite.

2.2. Corrosion tests

All corrosion tests were conducted at room temperature in 1.0 wt% NaCl solution by dissolving analytical grade NaCl in double-distilled water. An ACM Gill AC potentiostat was used to measure the potentials and currents during the tests employing a 3-electrode configuration, i.e. the test specimen as the working electrode, a saturated calomel electrode (SCE) as the reference electrode and a platinum mesh as the auxiliary electrode.

Before corrosion tests, the nitrided and un-nitrided surfaces were slight polished using 1 µm diamond paste to remove surface contaminants resulting from nitriding and to further smoothen the surface. This was followed by ultrasonic cleaning in ethanol for 10 min. Then the specimen was masked by using an insulating lacquer to leave a test window of 10 mm x 10 mm which would be exposed to the solution.

Corrosion tests were conducted both potentiodynamically to measure the anodic polarisation curves of the specimens and potentiostatically to measure the current evolution as a function of time at constant potentials. The potentiodynamic test was conducted at a scan rate of 1 mV/s, by sweeping potential from -200 mV (vs. open circuit potential (OCP)) to 800 mV (vs. OCP). The potentiostatic tests were conducted at a cathodic potential of -700 mV(SCE), at OCP, and at an anodic potential of -200 mV(SCE). During all the tests, the current and potential values were recorded continuously at a sampling rate of 1 Hz.

2.3. Tribocorrosion tests

Preprints (www.preprints.org) | NOT PEER-REVIEWED | Posted: 29 May 2023 doi:10.20944/preprints202305.2018.v1

Tribocorrosion tests were carried out under the same electrochemical conditions and following the same surface preparation procedures as those used in the corrosion tests described in section 2.2. A laboratory scale reciprocating wear test machine was used to perform the tests [31]. The incorporation of an electrochemical potentiostat with the tribometer allowed for the measurements of potential and current during the sliding wear process. Before the test, the specimen was masked by using an insulating lacquer to leave a test window of 15 mm x 3 mm which would be exposed to the solution. An electrically conducting lead was connected to the specimen to ensure conductivity of the specimen for electrochemical measurements. In order to ensure that electrochemical reactions only occur to the test window, all other fixtures, including the specimen holder, the test cell and the slider holder were made of nylon.

During tribocorrosion testing, the specimen was immersed in the 1.0 wt% NaCl solution. An SCE and a platinum wire were also inserted in the solution as the reference and auxiliary electrode respectively. An alumina (Al_2O_3) ball of 8 mm diameter (R_a=0.05 μm) was used as the stationary slider, which made sliding contact with the reciprocating specimen, generating a sliding track on the specimen. All tests were implemented under a contact load of 4 N for a total sliding duration of 7200 s at a reciprocating frequency of 1 Hz and an amplitude of 6 mm. Before and after sliding, the specimen was stabilized in the solution for 300 s under respective conditions, such that potentials and/or currents could be measured before, during and after sliding.

All corrosion and tribocorrosion tests were repeated twice and the average results are presented. Table 2 summarizes the test conditions under both sliding (tribocorrosion) and no-sliding (corrosion) conditions.

Table 2. Summary of corrosion and tribocorrosion conditions.

	Corrosion	Tribocorrosion
Potentiodynamic	-200 mV to 800 mV, 1 mV/s No sliding	-200 mV to 800 mV, 1 mV/s Sliding at 4 N & 1 Hz
Potentiostatic	-700 mV(SCE) no sliding OCP no sliding -200 mV(SCE) no sliding	-700 mV(SCE) sliding at 4 N & 1 Hz OCP sliding at 4 N and 1 Hz -200 mV(SCE) sliding at 4 N & 1 Hz

2.4. Specimen characterisation

After corrosion and tribocorrosion tests, the corroded surfaces and sliding tracks were examined microscopically under optical (Nikon LV150N) microscope and scanning electron microscope (SEM) (Carl Zeiss EVO LS 15). Using the extended-depth-of-focus feature of the Nikon microscope, 3D images and surface profiles of the sliding tracks could be captured. The SEM was equipped with EDX facilities for elemental composition analysis. A Taylor-Hobson profilometer (Surtonic Intra Touch) was used to measure the surface profiles across each sliding track at three locations to measure the cross-sectional area of the track and thus obtain the total material removal (TMR) from each specimen due to tribocorrosion.

3. Results

3.1. Potentiodynamic tests

Figure 2a shows the anodic polarisation curves measured without sliding and during sliding for the un-nitrided (raw) and plasma nitrided (PN) specimens. Under the condition of corrosion (no-sliding), the raw specimen showed active anodic dissolution behaviour: the current density increased quickly at anodic potentials above the corrosion potential and then increased slowly due to transpassivity. Microscopic examination revealed that the raw specimen suffered from severe corrosion which etched the grain structures and led to grain detachment (see Figure 3a). Under the same no-sliding condition, the PN specimen showed a higher corrosion potential and much lower current densities in the anodic region. The corroded area only showed some discolouration as compared to the

Preprints (www.preprints.org) | NOT PEER-REVIEWED | Posted: 29 May 2023 doi:10.20944/preprints202305.2018.v1

un-corroded area (see Figure 3b). Thus, in the test solution, the raw specimen was in the active state in the anodic region, while the γ′-Fe_4N layer formed on the surface by nitriding was effective in reducing the dissolution rate of mild steel. Under the condition of tribocorrosion (sliding), the corrosion potentials of both specimens were shifted cathodically and the current densities in the anodic region were increased (Figure 2a). This demonstrates that the sliding mechanical action activated both the raw surface and PN surface such that corrosion in the sliding tracks was accelerated, which is a common phenomenon observed in tribocorrosion [23,24,25].

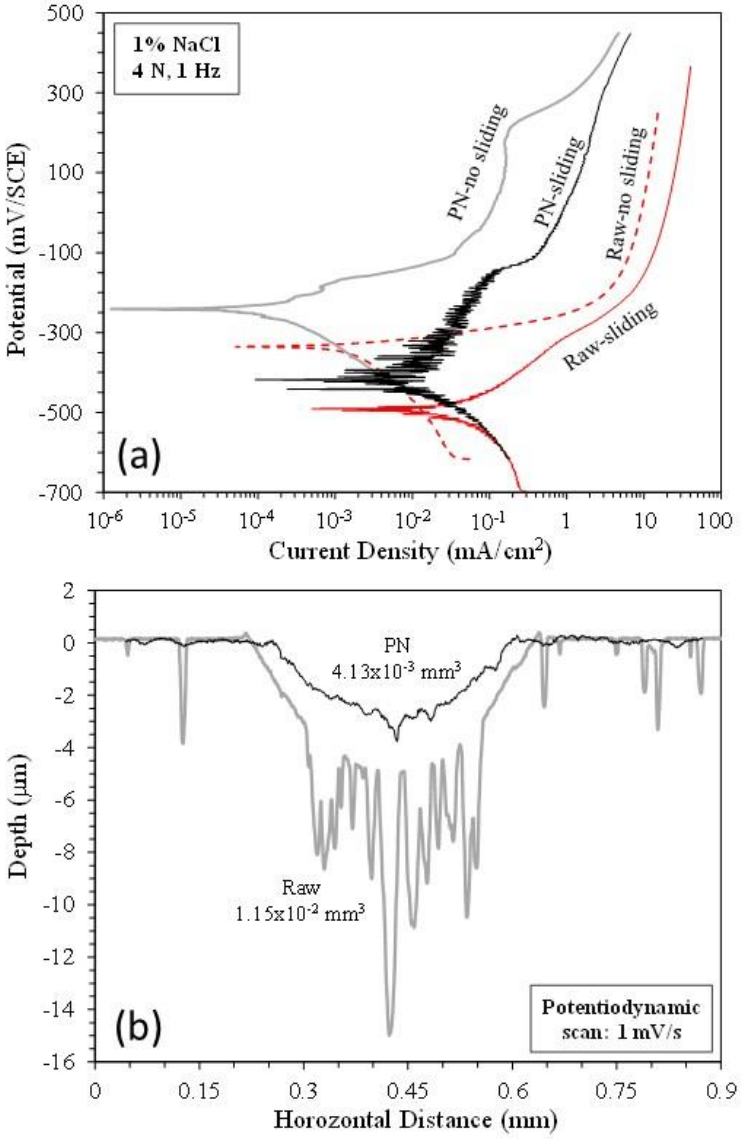

Figure 2. (a) Anodic polarisation curves measured without sliding and during sliding and (b) surface profiles measured across the sliding tracks produced during anodic polarisation.

Table 3 lists the corrosion potentials and corrosion current densities derived from the polarisation curves shown in Figure 2a. It can be seen that sliding led to an increase in corrosion current density by an order of magnitude for the raw specimen and by nearly two orders of magnitude for the PN specimen. As compared to the raw specimen, the PN specimen showed higher corrosion potentials and lower corrosion current densities, demonstrating that the γ′-Fe_4N layer had the ability to reduce corrosion under both sliding and no-sliding conditions.

Table 3. Corrosion potential (E_{corr}) and corrosion current density (i_{corr}) derived from the polarisation curves in Figure 2a.

Preprints (www.preprints.org) | NOT PEER-REVIEWED | Posted: 29 May 2023 doi:10.20944/preprints202305.2018.v1

	E_{corr} (mV/SCE)		i_{corr} (mA/cm^2)	
Specimen	No sliding	Sliding	No sliding	Sliding
Raw MS	-335	-490	$4.28x10^{-3}$	$4.95x10^{-2}$
PN MS	-241	-418	$2.05x10^{-4}$	$1.91x10^{-2}$

Figure 2b shows the surface profiles measured across the sliding tracks after anodic polarisation tests during sliding. It can be seen that the sliding track on the raw specimen was much deeper and rougher than that on the PN specimen. Material removal from outside the sliding track of the raw specimen was also evident, obviously due to corrosion occurring outside the sliding track, as can be seen from Figure 3c. The deep valleys in the sliding track shown in Figure 2b for the raw specimen were the results of accelerated corrosion. On the other hand, the sliding track on the PN specimen exhibited a shiny and polished appearance (Figure 3d). The TMR from the PN specimen was 64% smaller than that from the raw specimen (Figure 2b). The measured surface profile shown in Figure 2b also revealed that the sliding track on the PN specimen was smaller than 4 μm, thus tribocorrosion occurred mainly within the γ′-Fe_4N layer. However, some pits of several tens of microns in size were observed in the sliding track (Figure 3d&e). The penetration depth of the pits was as deep as 15 μm (Figure 3f), suggesting that once the γ′-Fe_4N layer was broken down locally, accelerated corrosion happened in the form of pitting corrosion during the tribocorrosion process.

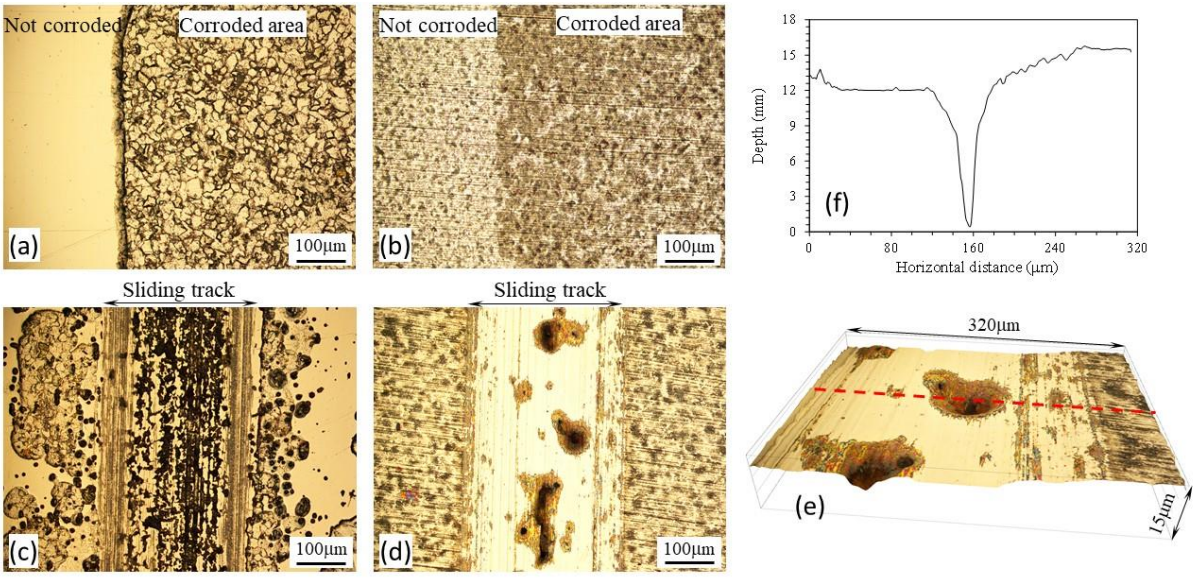

Figure 3. Microscopic images showing the test surfaces after potentiodynamic polarisation tests without sliding and during sliding: (a) raw MS without sliding, (b) PN MS without sliding, (c) raw MS with sliding, (d) PN MS with sliding, (e) 3D view of corrosion pits in (d), and (f) surface profile measured across a pit shown by the dashed line in (e).

The results presented in this section provides a general picture of the corrosion and tribocorrosion behaviour of the specimens over a wide potential range. In order to further demonstrate the beneficial effect of the γ′-Fe_4N layer in improving the tribocorrosion behaviour of mild steel, detailed tests were conducted potentiostatically at different potentials, as discussed in the following sections.

3.2. Cathodic potential tests

Figure 4a shows the recorded current versus time curves at the cathodic potential of -700 mV(SCE) under both sliding and no-sliding conditions. Under no-sliding conditions, negative currents were recorded for both specimens, suggesting that cathodic reactions were dominant, while metal oxidation (corrosion) became less dominant [23]. Sliding led to an increase in cathodic current from around -0.04 mA to around -0.1 mA for both

Preprints (www.preprints.org) | NOT PEER-REVIEWED | Posted: 29 May 2023 doi:10.20944/preprints202305.2018.v1

specimens, suggesting that the sliding action activated the surfaces and accelerated cathodic reactions.

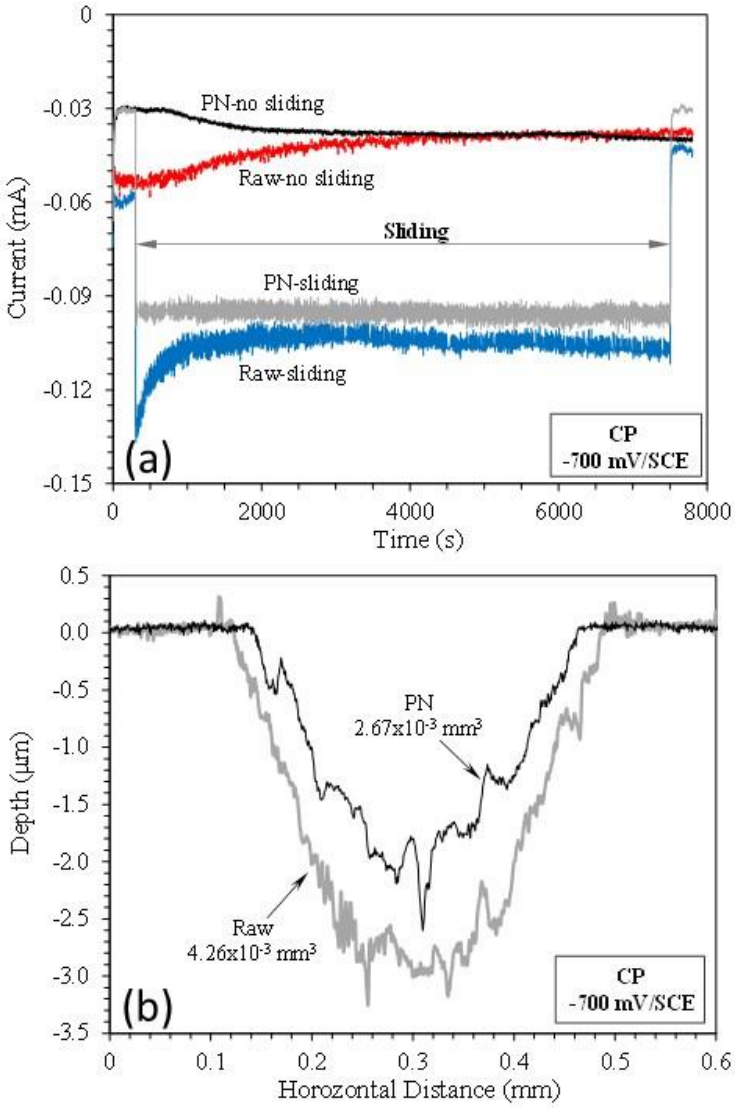

Figure 4. (a) Current variation with time measured without sliding and during sliding at the cathodic potential of -700 mV(SCE) and (b) surface profiles measured across the sliding tracks produced by sliding at -700 mV(SCE) (b).

Although corrosion is still possible at such a cathodic potential, its contribution to TMR from the sliding track is insignificant [23,31]. Thus, TMR was mainly due to mechanical wear. Figure 4b shows the surface profiles measured across the sliding tracks on the raw and PN specimens. It can be seen that the sliding track on the raw specimen was deeper and wider than that on the PN specimen. The wear depth on the PN specimen was smaller than 3 μm, thus wear occurred within the 5 μm thick γ′-Fe_4N layer. The TMR from the PN specimen was about 63% of that from the raw specimen. Clearly, the γ′-Fe_4N layer had the ability to reduce mechanical wear of mild steel by about 37%.

Figure 5 shows the SEM images and EDX elemental mappings of the sliding tracks on the raw and PN specimens. The parallel scratch marks on the sliding tracks are good indications of mechanical abrasion wear arising from the sliding action of the alumina slider. The sliding track on the PN specimen showed a shiny appearance with very few signs of corrosion (Figure 5b). EDX mapping could not find oxygen on the worn surface, instead, nitrogen was found (Figure 5b), furthering confirming that the γ′-Fe_4N layer was not worn through. On the other hand, the sliding track on the raw specimen was covered

Preprints (www.preprints.org) | NOT PEER-REVIEWED | Posted: 29 May 2023 doi:10.20944/preprints202305.2018.v1

with some dark grey products, which were rich in oxygen (Figure 5a), suggesting that limited corrosion could happen to the raw specimen at such a cathodic potential.

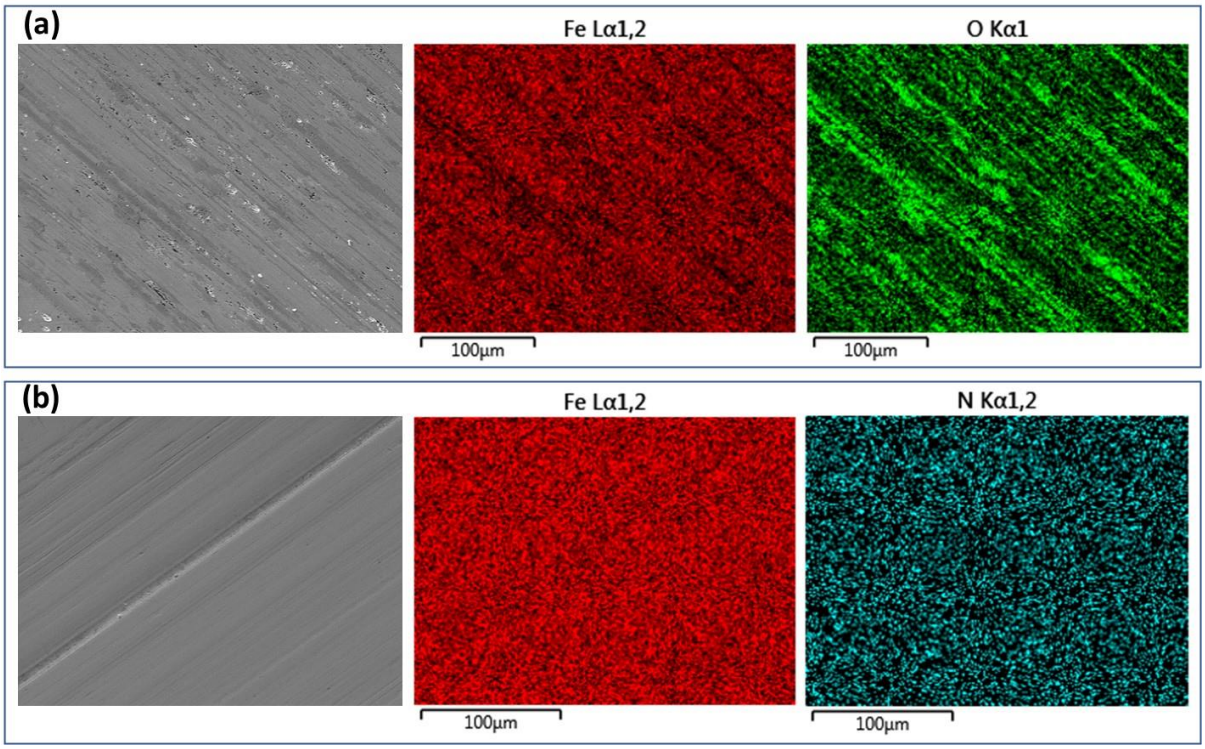

Figure 5. Microscopic images and EDX mapping of the sliding tracks produced at the cathodic potential of -700 mV(SCE) on the (a) raw MS and (b) PN MS specimens.

3.3. Open circuit potential (OCP) tests

The OCP versus time curves recorded under open circuit conditions are shown in Figure 6a. Under no-sliding conditions, OCP of both specimens decreased with increasing time of immersion in the solution. Both specimens were in the active state such that the surfaces became more activated with increasing time of immersion, leading to decreased OCP values. Under sliding conditions, the recorded OCP values also decreased with time and were more negative than those measured under no-sliding conditions, suggesting that sliding led to further activation of the surfaces. In agreement with the potentiodynamic measurements shown in Figure 2a, the OCP values measured for the PN specimen were more anodic than those measured for the raw specimen under both sliding and no-sliding conditions. Clearly, the raw surface was in a more active state than the PN surface under open circuit condition.

The surface profiles measured across the sliding tracks are shown in Figure 6b. The sliding track on the raw specimen was deeper than that on the PN specimen. Interestingly, material removal also occurred outside the sliding track on the raw specimen, which was due to corrosion in areas exposing to the solution outside the track, as can be seen from Figure 7a. On the other hand, corrosion outside the sliding track on the PN specimen was very limited (Figure 6b), which was confirmed by microscopic examination (Figure 7c). Inside the sliding track, there were clear signs of corrosion in addition to the parallel abrasion marks (Figure7 b&d). The wear depth of the PN specimen was smaller than 5 μm (Figure 6b), thus wear and corrosion occurred within the γ'-Fe_4N layer. A few pits were also observed inside the sliding track on the raw specimen, where were several microns in depth (Figure 7b).

TMRs from the specimens were obviously the combined results of wear (abrasion) and corrosion. TMR from the PN specimen was about 35% smaller than that from the raw specimen (Figure 6b). When compared with TMRs resulting from sliding at the cathodic

Preprints (www.preprints.org) | NOT PEER-REVIEWED | Posted: 29 May 2023 doi:10.20944/preprints202305.2018.v1

potential of -700 mV(SCE) discussed in Section 3.2, TML at OCP was 2.8 times larger for the raw specimen and 3.6 larger for the PN specimen. This demonstrates the effect of corrosion and corrosion-wear synergism in accelerating TMR from the specimen.

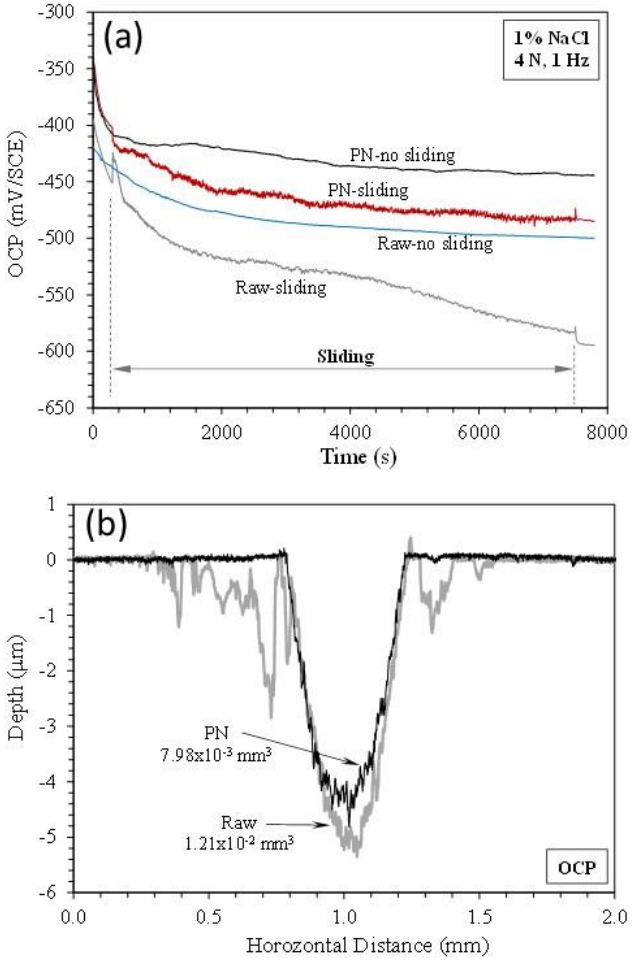

Figure 6. (a) Open circuit potential (OCP) variation with time measured without sliding and during sliding at OCP and (b) surface profiles measured across the sliding tracks produced by sliding at OCP.

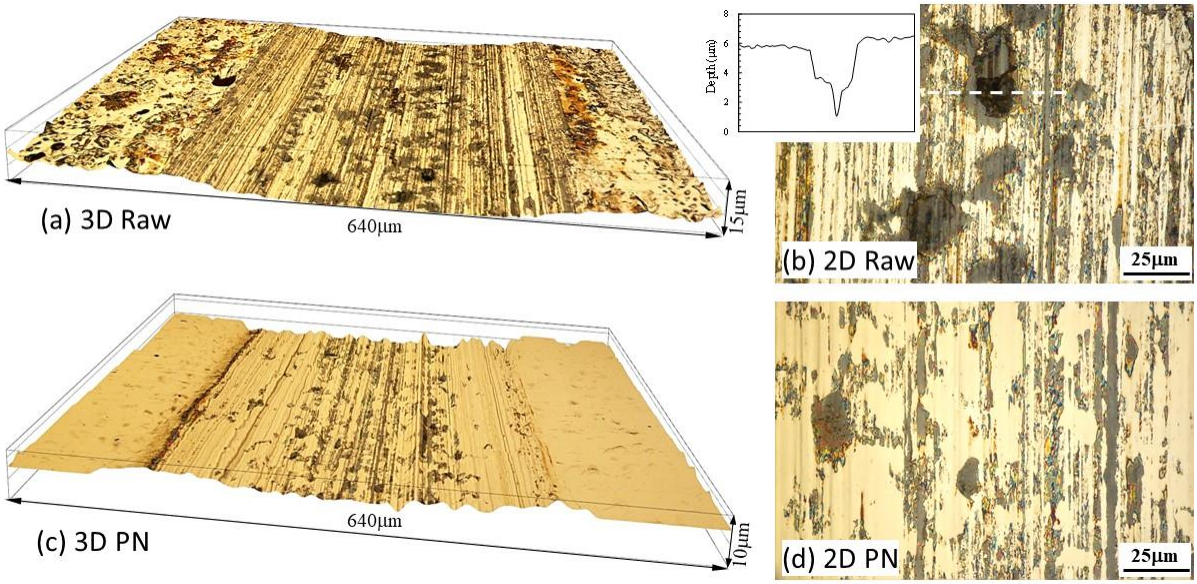

 doi:10.20944/preprints202305.2018.v1

Figure 7. Microscopic images showing 3D (a & c) and 2D (b & d) views of the sliding tracks produced at OCP on the raw MS (a & b) and PN MS (c & d) specimens. The inset in (b) shows the surface profile measured across the pit indicated by the dashed line.

3.4. Anodic potential tests

At the anodic potential of -200 mV(SCE), the raw and PN specimens behaved quite differently (Figure 8a). Under no-sliding conditions, both the raw and PN specimen registered continuously increasing current with polarisation time, confirming that the specimens suffered from anodic dissolution and had no ability to passivate at such an anodic potential. However, the current generated from the PN specimen was more than two orders magnitude smaller than that generated from the raw specimen (Figure 8a&b), demonstrating that the γ′-Fe_4N layer had the ability to reduce metal dissolution and improve corrosion resistance.

Interestingly, sliding led to a decrease in current from the raw specimen (Figure 8a), which is different from the observations made on passive metals where sliding leads to an abrupt increase in current due to the depassivation of the surface by the sliding action [24,25,31]. For the active raw specimen in this study, removal of the corrosion products from the sliding track by the mechanical action obviously helped to reduce metal dissolution. After the termination of sliding, the current from the raw specimen increased to the level measured under no-sliding condition. Microscopic examination revealed that corrosion occurred both inside and outside the sliding track of the raw specimen (Figure 9). Outside the sliding track, the surface became quite rough with peaks and valleys due to grain detachment arising from the corrosion action (Figure 9b. Inside the sliding track, the peaks were flattened due to the wearing action, but the valleys and some corrosion pits could still be observed (Figure 9a).

On the other hand, sliding led to an abrupt increase in current from the PN specimen, and the current generated during sliding increased slowly for the first 2000 s, and then increased more quickly between 2000 s and 4000 s sliding, and then further quickly after 4000 s sliding (Figure 8b). Microscopic examination (Figure 10) revealed that in the central region of the sliding track on the PN specimen, the γ′-Fe_4N layer was removed, such that pits were formed in this region, which penetrated deep into the substrate (Figure 8c and Figure 10). This explains the quick increase in current after 2000 s and then 4000 s sliding (Figure 8b).

Preprints (www.preprints.org) | NOT PEER-REVIEWED | Posted: 29 May 2023 doi:10.20944/preprints202305.2018.v1

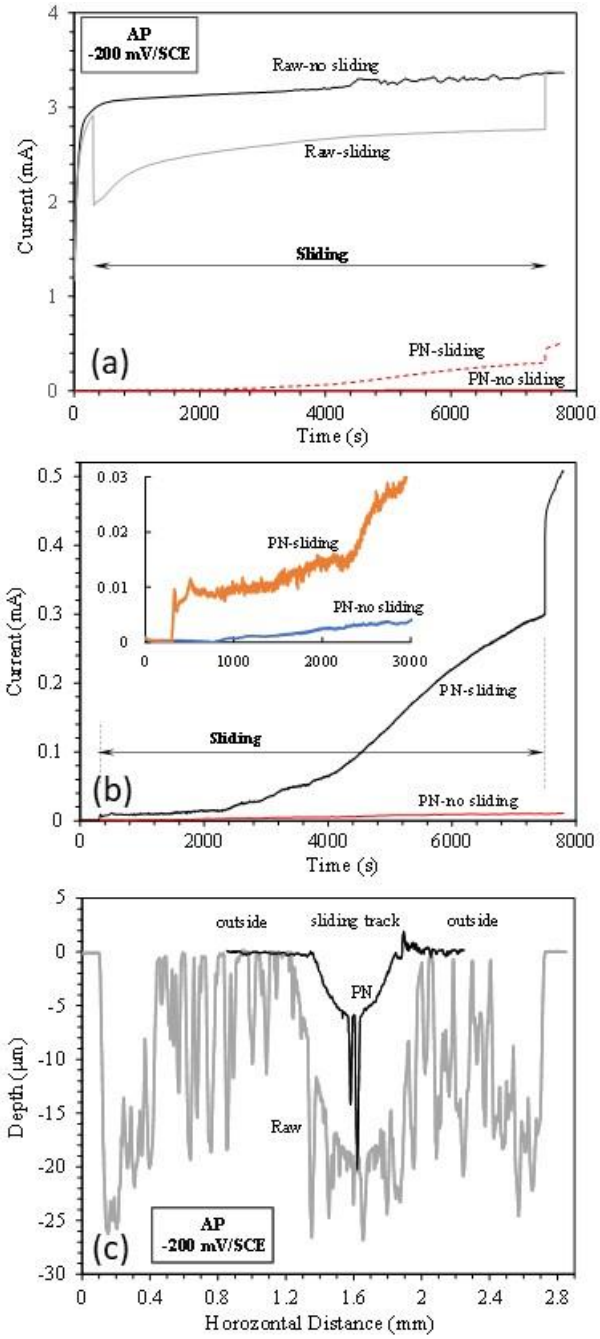

Figure 8. (a) Current variation with time measured without sliding and during sliding at the anodic potential of -200 mV(SCE), (b) zoom-in view of current variation of the nitrided specimen during sliding at -200 mV(SCE) and (c) surface profiles measured across the sliding tracks produced by sliding at -200 mV(SCE).

Surface profile measurements across the sliding tracks showed that TMR from the PN specimen was mainly from the sliding track with limited corrosion loss outside the sliding track (Figure 8c). The wear depth in the central region of the sliding track was more than 5 μm and as deep as 20 μm in the pitting area, suggesting that the γ'-Fe_4N layer was worn through in this region, in line with the microscopic examination (Figure 10). On the other hand, for the raw specimen, TMR came from both inside and outside the sliding track (Figure 8c). Thus, corrosion played a more significant role in TMR from the raw specimen.

Preprints (www.preprints.org) | NOT PEER-REVIEWED | Posted: 29 May 2023 doi:10.20944/preprints202305.2018.v1

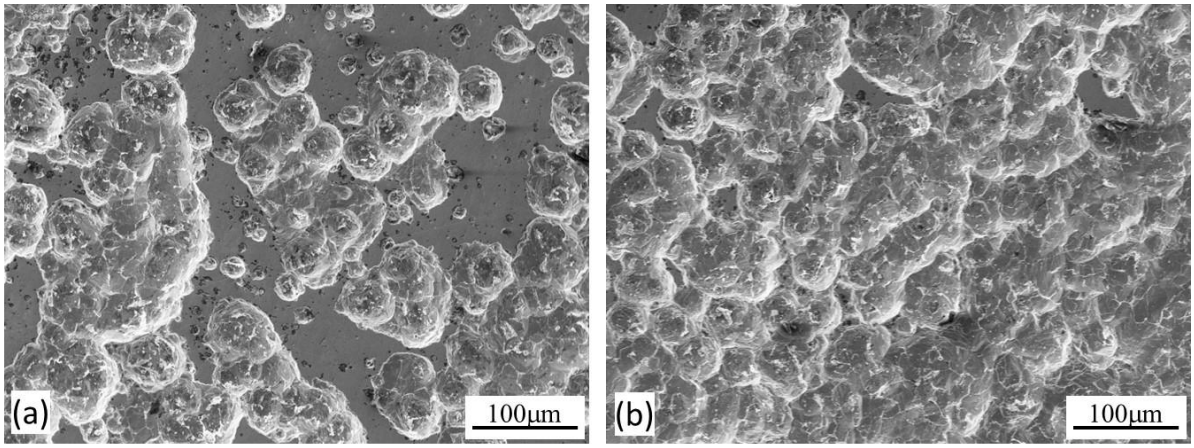

Figure 9. Microscopic images showing (a) the worn surface inside the sliding track and (b) the corroded surface outside the sliding track, produced at the anodic potential of -200 mV(SCE) on the raw MS.

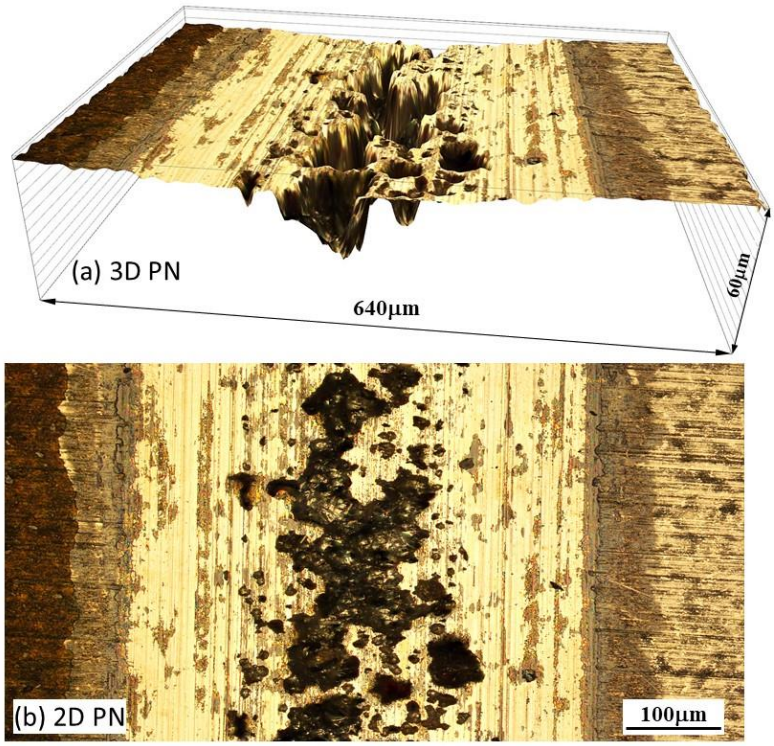

Figure 10. Microscopic images showing (a) 3D and (b) 2D views of the sliding track, produced at the anodic potential of -200 mV(SCE) on the PN MS.

4. Discussion

4.1. Effect of potential on tribocorrosion behaviour

From the results presented in Section 3, the 5 μm γ′-Fe_4N thick layer was not worn through during the tribocorrosion tests. Thus, the measured corrosion and tribocorrosion behaviour of the nitride specimen is characteristic of the γ′-Fe_4N layer. It is clear that the γ′-Fe_4N layer produced by nitriding on mild steel has the ability to increase surface hardness, reduce metal dissolution rate and improve tribocorrosion resistance in the NaCl containing solution. The tribocorrosion behaviour of the γ′-Fe_4N layer is affected by the applied potential, as summarised in Figure 11, which shows the variation of average coefficient of friction (COF) and TMR with potential.

Preprints (www.preprints.org) | NOT PEER-REVIEWED | Posted: 29 May 2023 doi:10.20944/preprints202305.2018.v1

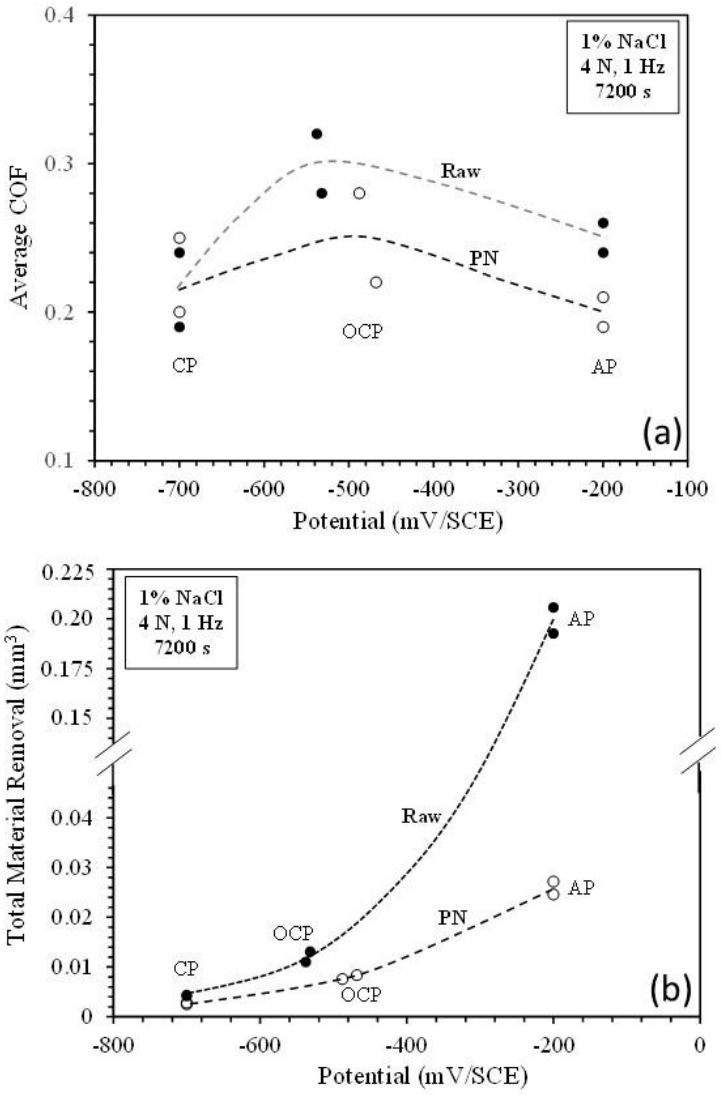

Figure 11. (a) Average coefficient of friction (COF) and (b) total material removal during sliding at cathodic (CP), open circuit (OCP) and anodic (AP) potentials.

The COF values vary quite largely between two repeated tests under the same conditions (Figure 11a). However, a general trend can be seen that the average COF for both specimens is the highest at OCP and is lower at cathodic and anodic potentials. This behaviour can be explained as follows. At the cathodic potential of -700 mV(SCE), mechanical wear is predominant and there is little contribution of corrosion products to friction. At OCP, both mechanical wear and chemical wear are involved and there is synergism between wear and corrosion, which could lead to increased friction because of the trapping of corrosion wear products at the frictional interface. At the anodic potential of -200 mV(SCE), although corrosion is accelerated, the formation of corrosion pits, particularly at the central region of the sliding track on the PN specimen (Figure 10), could reduce the real contact area and thus could lead to reduced friction. As compared to the raw specimen, the PN specimen shows lower friction at OCP and -200 mV(SCE), thus the γ′-Fe_4N layer is beneficial in reducing friction during tribocorrosion in the NaCl containing solution.

The variation of TMR with potential is shown in Figure 11b. It can be seen that the TMR of both specimens increases with potential and the TMR of the PN specimen is significantly lower than that of the raw specimen under all test conditions. As the potential is increased from OCP to -200 mV(SCE), the TMR of the raw specimen is increased by nearly 17 times, while the TMR of the PN specimen is increased only by 3 times. When

Preprints (www.preprints.org) | NOT PEER-REVIEWED | Posted: 29 May 2023 doi:10.20944/preprints202305.2018.v1

comparing the TMR of the two specimens, the TMR of the PN specimen is 37% lower at the cathodic potential, 35% lower at OCP and 87% lower at the anodic potential than the raw specimen. This demonstrates the beneficial effect of the γ′-Fe_4N layer on improving the resistance to mechanical wear and chemical wear of mild steel, as discussed below.

4.2. Contribution of mechanical wear and chemical wear

Material removal is the result of mechanical wear and chemical wear. At the cathodic potential, corrosion is limited and mechanical wear is dominant. The results (Figure 4b and Figure 11b) show that the TMR of the PN specimen is 37% smaller than that of the raw specimen. This can be attributed to the high hardness of the γ′-Fe_4N layer (Table 1), which provides good resistance to mechanical abrasive wear. At OCP and the anodic potential, both mechanical and chemical wear are involved and there is synergism between wear and corrosion. The *TMR* is the sum of material removal due to mechanical wear (V_{mech}) and chemical wear (V_{chem}) [22,32], i.e.

$$TMR = V_{mech} + V_{chem} \quad (1)$$

where TMR can be measured after the tests (e.g. Figure 11b) and V_{chem} can be theoretically estimated by using the Faraday's law [24,33]:

$$V_{chem} = \frac{ItM}{nF\rho} \quad (2)$$

where I is the corrosion current (A) evolved during sliding, t (s) is the sliding time, M (g/mol) is the atomic mass of the steel, n is the valence of oxidation, which is 3 to account for FeOOH oxide film on steel, which is the main corrosion product of carbon steel [34,35], F is the Faraday's constant (96,458 C/mol) and ρ is the density of steel.

Equation (2) can be used to calculate V_{chem} if general corrosion is the predominant form of corrosion. In the present work, at the anodic potential of -200 mV(SCE), significant pitting corrosion occurred inside the sliding track (Figure 9 and 10), particularly in the central region of the sliding track on the PN specimen, thus most of the measured currents (Figure 8a&b) are expected to come from the corrosion pits. In such a case, it is unrealistic to estimate V_{chem} by using Equation (2). However, at OCP, general corrosion was predominant, thus the corrosion parameter data shown in Table 3 can be used to estimate V_{chem} for both specimens, and then Equation (1) can be used to calculate V_{mech}. The results are summarised in Table 4.

From Table 4, it can be seen that at OCP, chemical wear accounts for 48% of TMR from the raw specimen, while it accounts for only 28% of TMR from the PN specimen. At OCP, mechanical wear from the PN specimen is also smaller than that from the raw specimen. Thus, the γ′-Fe_4N layer indeed has the ability to provide improved resistance to both chemical wear and mechanical wear, obviously due to its high hardness and good corrosion resistance. It is also evident that the γ′-Fe_4N layer is particularly good in reducing chemical wear, which contributes significantly to the reduction in TMR from the PN specimen.

Table 4. Summary of TMR, V_{mech} and V_{chem} at OCP.

Specimen	TMR (mm^3)	V_{mech} (mm^3)	V_{chem} (mm^3)	% of V_{chem}
Raw	1.204×10^{-2}	6.265×10^{-3}	5.775×10^{-3}	48
PN	7.983×10^{-3}	5.755×10^{-3}	2.228×10^{-3}	28

Although it is not possible to quantitatively estimate the relative contribution of chemical wear and mechanical wear at the anodic potential by using Equation (2), judging from the measured currents (Figure 8) and sliding track morphology (Figure 9 and 10), it can be deduced that chemical wear plays an increasing role in TMR from both specimens. For the PN specimen, the local breakdown of the γ′-Fe_4N layer can lead to much accelerated corrosion in the form of pitting corrosion, which in term can lead to accelerated mechanical wear [36]. Thus, like other surface coatings for corrosion and wear protection,

 doi:10.20944/preprints202305.2018.v1

there is always an issue concerning the sustainability of the coating system under harsh loading and environmental conditions [37].

5. Conclusions

1. In the NaCl containing solution, both the raw mild steel and γ′-Fe_4N layer are in the active state in the anodic region. The γ′-Fe_4N layer has the ability to reduce metal dissolution and improve corrosion resistance of mild steel.
2. At the cathodic potential, where mechanical wear dominates, the γ′-Fe_4N layer can reduce total material removal by 37% due to its higher hardness than that of raw mild steel.
3. At open circuit potential, where both mechanical wear and chemical wear are involved, the γ′-Fe_4N layer has the ability to reduce chemical wear due to its better resistance to metal dissolution, such that the total material removal is reduced by 35% as compared to that from the raw mild steel.
4. At the anodic potential, where chemical wear plays an increasing role, the γ′-Fe_4N layer can reduce total material removal by 87%. However, local breakdown of the γ′-Fe_4N layer can happen in the sliding track, leading to accelerated pitting corrosion.
5. The γ′-Fe_4N layer has the ability to improve the tribocorrosion behaviour of mild steel in the NaCl containing solution under all test conditions. But there is a concern regarding the sustainability of the layer when localised breakdown or wearing-through occurs, which can lead to accelerated pitting and accelerated material removal.

References

1. Staines, A.M.; Bell, T. Technological importance of plasma-induced nitrided and carburized layers on steel. *Thin Solid Films* **1981**, 86, 201–212.
2. Spies, H.J.; Thien, H.L.; Biermann, H.B. Controlled nitriding. *Metal Science and Heat Treatment* **2004**, 46, 272–276.
3. B.J. Lightfoot, B.J.; Jack, D.H. Kinetics of nitriding with and without white-layer formation. *Heat Treatment '73*, The Metals Society, December **1973** (republished in the Source Book on Nitriding, American Society for Metals, Metals Park, Ohio, **1977**, pp.248–254).
4. Thermochemical Surface Engineering of Steels. Edited by Mittemeijer, E.J; Somers, A.L. **2015**, Elsevier.
5. Menthe, E.; Rie, K.T.; Schultze, J.W.; Simson, S. Structure and properties of plasma-nitrided stainless steel. *Surface and Coatings Technology* **1995**, 74-75, 412–416.
6. Zhang, L.; Shao, M.; Zhang, Z.; Yi, X.; Yan, J.; Zhou, Z.; Fang, D.; He, Y.; Li, Y. Corrosion behaviour of nitrided layer of Ti6Al4V titanium alloy by hollow cathodic plasma source nitriding. *Materials* **2023**, 16, 2961.
7. Zhecheva, A.; Malinov, S. Titanium alloys after surface gas nitriding. *Surface and Coatings Technology* **2006**, 201, 2467–2474.
8. Buchwalder, A.; Bocker, J.; Hegelmann, E.; Klemm, V. Investigations on the microstructure of an aluminium nitride layer and its interface with the aluminium substrate (Part I). *Coatings* **2022**, 12, 618.
9. Visuttipitukul, P.; Aizawa, T.; Kuwahara, H. Advanced plasma nitriding for aluminium and aluminium alloys. *Materials Transactions* **2003**, 44, 2695–2700.
10. Sun, Y. Kinetics of layer growth during plasma nitriding of nickel based alloy Inconel 600. *Journal of alloys and compounds* **2003**, 351, 241-247.
11. Tao, X.; Kavanagh, J.; Li, X.; Dong, H.; Matthews, A.; Leyland, A. An investigation of precipitation strengthened Inconel 718 superalloy after triode plasma nitriding. *Surface and Coatings Technology* **2022**, 442, 128401.
12. Luo, X.; Li, X.; Sun, Y.; Dong, H. Tribocorrosion behaviour of S-phase surface engineered medical grade Co-Cr alloy. *Wear* **2013**, 302, 1615-1623.
13. Purandare, Y.; Shukla, K.; Sugumaran, A.; Ehiasarian, A.; Khan, I.; Hovsepian, P. Improving tribocorrosion resistance of a medical grade CoCrMo alloy by the novel HIPIMS nitriding technique. *Journal of Science: Advanced Materials and Devices* **2023**, 8, 100570.
14. Spies, H.J. Corrosion behaviour of nitrided, nitrocarburised and carburised steels, in *Thermochemical Surface Engineering of Steels*, edited by Mittemeijer, E.J; Somers, A.L. **2015**, Elsevier.
15. Mittemeijer, E.J. Nitriding of binary and ternary iron-based alloy. in *Thermochemical Surface Engineering of Steels*, edited by Mittemeijer, E.J; Somers, A.L. **2015**, Elsevier.
16. Jasinski, J.J; Kurpaska, L.; Frazek, T.; Lubas, M.; Sitarz, M. Structural characterisation of fine γ′-Fe_4N nitrides form by active screen plasma nitriding. *Metals* **2020**, 10, 1656.
17. Bell, T.; Loh, N.L. The fatigue characteristics of plasma nitrided three Pct Cr-Mo steel. *Journal of Heat Treating* **1982**, 2, 232–237.

`

18. Kato, H.; Eyre, T.S.; Ralph, B. Wear mechanism map of nitrided steel. *Acta Metallurgica et Materialia* **1994**, 42, 1703–1713.
19. Bell, T.; Sun, Y. Load bearing capacity of plasma nitrided low alloy steel under combined rolling-sliding contact. *Surface Engineering* **1990**, 6, 133-139.
20. Boztepe, E; Alves, A.C; Ariza, E; Rocha, L.A.; Cansever, N.; Toptan, F. A comparative investigation of the corrosion and tribocorrosion behaviour of nitrocarburized, gas nitrided, fluidized-bed nitrided, and plasma nitrided plastic mould steel. *Surface & Coatings Technology* **2018**, 334, 116–123.
21. Ram Mohan Rao, K.; Nouveau, C; Lakshman, S.; Muralidhar, P.; Trinadh, K. Effect of low and high temperature plasma nitriding on electrochemical corrosion of steel. *Materials Today: Proceedings* **2020**, 39, 1367–1371.
22. Valdes, J.; Huape, E.; Oseguern, J.; Ruiz, A.; Ibarrra, J.; Bernal, J.L.; Medina, A. Effects of plasma nitriding in corrosion behaviour of an AISI 4140 steel using a seawater medium solution. *Materials Letters* **2022**, 316, 131991.
23. S.W. Watson, F.J. Friedersdorf, B.W. Madsen, S.D. Gramer, Methods of measuring wear-corrosion synergism, Wear, 1995, 181-183, p476-484.
24. P. Ponthiaux, F. Wenger, D. Drees, J.P. Celis, Electrochemical techniques for studying tribocorrosion processes, Wear, 2004, 256, 459–468.
25. A.I. Munoz, N. Espallargas, S. Mischler, Ed., Tribocorrosion, Springer, 2020.
26. Mindivan, F.; Aktas, G.R.; Bayram, A. Influence of plasma nitriding on dry wear, corrosion and tribocorrosion performance of 17-4 precipitation hardening stainless steel. *Materialwiss. Werkstofftech* **2022**, 53, 963–978.
27. Li. X.; Dou, W.; Tian, L.; Dong, H. Combating the tribo-corrosion of LDX2404 lean duplex stainless steel by low temperature plasma nitriding. *Lubricants* **2018**, 93, 1–12.
28. Hacisalihoglu, I.; Yildiz, F.; Celik, A. Tribocorrosion behavior of plasma nitrided Hardox steels in NaCl solution. *Tribology International* **2018**, 120, 434–445.
29. Wong-Angel, W.D.; Martinez-Trinidad, J.; Campos-Silva, V.; Hernandez-Hernandez; Silva-Rivera, U.S.; Garcia-Leon, R.A. Wear-corrosion synergy on Din-16MnCr5 steel under nitriding and post-oxidizing treatments. *Journal of Bio- and Tribo-Corrosion* **2021**, 7, 83.
30. Takahashi, T.; Burghaus, J.; Music, D.; Dronskowski, R.; Schneider, J.M. Elastric properties of γ′-Fe_4N probed by nanoindentation and ab initio calculation. *Acta Materialia* **2012**, 60, 2054-2060.
31. Sun, Y.; Bailey, R. Comparison of wear performance of low temperature nitrided and carburized 316L stainless steel under dry sliding and corrosive-wear condition. *J Mater Eng Perform.* **2022**, https://doi.org/10.1007/s11665-022-07182-9.
32. Casar, J.; Malia, B.; Mazzonello, A.; Karl, A.; Buhagiar, J. Improved tribocorrosion resistance of a CoCrMo implant material by carburising. *Lubricants* **2018**, 6, 76.
33. Rasool, G.; Shafei, Y.E.; Stack, M.M. Mapping tribo-corrosion behaviour of Ti-6Al-4V Eli in laboratory simulated hip joint environments. *Lubricants* **2020**, 8, 69.
34. Antunes, R.A.; Ichikawa, R.U.; Martinez, L. G.; Costa, I. Characterisation of corrosion products on carbon steel exposed to natural weathering and to accelerated corrosion tests. *International Journal of Corrosion* **2014**, 2014, 419570.
35. Fonna, S.; Ibrahim, I.B.M.; Gunawarman; Huzni, S.; Lksan, M.; Thalib, S. Investigation of corrosion products formed on the surface of carbon steel exposed in Banda Aceh's atmosphere. *Heliyon* **2021**, 7, e06608.
36. Jiang, J.; Stack, M.M.; Neville, A. Modelling the tribo-corrosion interaction in aqueous sliding conditions. *Tribology International* **2002**, 35, 669-679.
37. Sun, Y.; Dearnley, P.A.; Bertram, M. Response of duplex Cr(N)/S and Cr(C)/S coatings on 316L stainless steel to tribocorrosion in 0.89% NaCl solution under plastic contact conditions. *Journal of Biomedical Materials Research, Part* B **2017**, 105, 1503-1513.